Insulator-to-metal Mott transition facilitated by lattice deformation in monolayer α-RuCl$_3$ on graphite

Xiaohu Zheng [1,*] Ogasawara Takuma,[1] Huaxue Zhou,[1] Chongli Yang,[1] Xin Han,[2]
Gang Wang,[3] Junhai Ren,[1] Youguo Shi,[2] Katsumi Tanigaki [1] and Rui-Rui Du[4,5]

[1]*Beijing Academy of Quantum Information Sciences, Beijing 100193, People's Republic of China*

[2]*Beijing National Laboratory for Condensed Matter Physics and Institute of Physics, Chinese Academy of Sciences,
Beijing 100190, People's Republic of China*

[3]*Department of Microelectronic Science and Engineering, School of Physical Science and Technology, Ningbo University,
Ningbo 315211, People's Republic of China*

[4]*International Center for Quantum Materials, School of Physics, Peking University, Beijing 100871, People's Republic of China*

[5]*CAS Center for Excellence in Topological Quantum Computation, University of Chinese Academy of Sciences,
Beijing 100190, People's Republic of China*

Creating heterostructures with graphene/graphite is a practical method for charge-doping α-RuCl$_3$, but not sufficient to cause the insulator-to-metal transition. In this study, detailed scanning tunneling microscopy/spectroscopy measurements on α-RuCl$_3$ with various lattice deformations reveal that both in-plane and out-of-plane lattice distortions may collapse the Mott gap in the case of monolayer α-RuCl$_3$ in proximity to graphite, but have little impact on its bulk form alone. In the Mott-Hubbard framework, the transition is attributed to the lattice-distortion-facilitated substantial modulation of the electron correlation parameter. Observation of the orbital textures on a highly compressed monolayer α-RuCl$_3$ flake on graphite provides valuable evidence that electrons are efficiently transferred from the heterointerface into Cl3p orbitals under the lattice distortion. It is believed that the splitting of Ru t_{2g} bands within the trigonal distortion of Ru-Cl-Ru octahedra bonds generated the electrons' transfer pathways. The increase of the Cl3p states enhances the hopping integral in the Mott-Hubbard bands, resulting in the Mott transition. These findings suggest a different route for implementing the insulator-to-metal transition upon doping in α-RuCl$_3$ by deforming the lattice in addition to the formation of the heterostructure.

I. INTRODUCTION

The Mott transition in materials with strong electron correlations is commonly referred to as a discontinuous phase transition (first order), during which both the spin and charge undergo substantial qualitative changes [1–3]. It ensures many intriguing physics such as high-temperature superconductivity (HTSC), strange metal phase, charge density wave (CDW), and other symmetry-broken states [4–7]. Cuprates that exhibit HTSC and charge order in the vicinity of a Mott transition are an established instance [8]. Under sufficiently strong spin-orbital coupling (SOC), Mott insulators can exhibit a quantum spin liquid (QSL) phase with topological order and fractional spinon excitation [9–12], providing a conductive environment for investigating a continuous Mott transition (second-order phase transition) with more intriguing physics [13,14]. By virtue of spin-dependent interactions among spin-half moments [15–17], the Kitaev honeycomb model admitting an exact QSL state and non-Abelian Majorana spinons stands out as a remarkable example. Numerous theoretical studies [18–20] have predicted that the Mott transition in such a

Kitaev QSL system could result in a rich phase diagram containing a p-wave topological superconducting phase. Charge doping is regarded as an efficient method for approaching such a Mott transition. Hitherto, a carrier-doped phase of the proximate Kitaev QSL material α-RuCl$_3$ has been studied by multiple research groups utilizing various strategies [21–24]. Comprising heterostructures of graphene/graphite appear to be the most advantageous among the options reported to date, due to the ability to prevent the introduction of crystal defects. Experimental evidence has provided empirical support for the notion that electrons, possessing a magnitude of 10^{13} cm^{-2}, can be transferred from graphene to α-RuCl$_3$, resulting in an equal amount of holes doping in graphene [23,25–28]. However, the insulator-to-metal transition accompanied by the emergence of a well-defined Fermi surface (FS) has not been observed in α-RuCl$_3$ yet, impeding further exploration of the potential superconductivity in this system.

In our recent study [29], we reported that the in-gap states of α-RuCl$_3$ in proximity to graphite sensitively experienced a notable augmentation upon the introduction of lattice distortion, which aligns with the theoretical anticipation that straining the lattice may be a powerful potential method for approaching the Mott transition in α-RuCl$_3$ [25,30,31]. Here, we use scanning tunneling microscopy/spectroscopy

---

*Corresponding author: xhzheng@baqis.ac.cn

035106-1

(STM/STS) to further explore the electronic properties of α-RuCl$_3$ with lattice deformations and strain at liquid nitrogen temperature (77 K). The experimental findings offer a significant clarification that the imposition of strain, regardless of whether it is compressive or extensive, in plane or out of plane, on the lattice of the monolayer (ML)-α-RuCl$_3$ transferred onto a graphite substrate may result in the insulator-to-metal Mott transition, while it has a negligible impact on the bulk form of α-RuCl$_3$. Upon subjecting the ML-α-RuCl$_3$ lattice to a uniform compression of 18%, we observe atomic-resolved orbital textures, which provide the evidence that newly arising low-energy electronic states in the Cl3p orbitals are responsible for the Mott transition. The proposed explanation posits that the lattice distortion has caused the splitting of the t_{2g} band, which provides the pathways for the electrons transferring from the heterointerface to the upper Cl3p orbitals. The new arising states effectively modulate the electron correlations in Mott-Hubbard bands in α-RuCl$_3$. These findings provide a prospective route for the manifestation of FS, thereby affording an opportunity to explore the phenomenon of topological superconductivity in the vicinity of a Mott transition within a Kitaev QSL.

II. RESULTS AND DISCUSSION

A. STM/STS on bulk α-RuCl$_3$ with film corrugations

α-RuCl$_3$ is an insulating 4d transition-metal halide with honeycomb layers composed of nearly ideal edge-sharing RuCl$_6$ octahedra [32], which can be exfoliated into a two-dimensional ML with a thickness of 600 pm [33], as depicted schematically in Fig. 1(a). As illustrated in the upper panel of Fig. 1(b), the crystal field of RuCl$_6$ octahedra splits the fivefold degenerate d levels of 4d^5 Ru^{3+} into the doublet e_g and the triplet t_{2g} with a charge gap exceeding 2 eV. The t_{2g} manifold composed of the d_{xy}, d_{yz}, and d_{xz} orbitals of Ru^{3+} hybridizes with the 3p (p_x, p_y, p_z) orbitals of Cl$^-$ [30,34]. Subsequently, the SOC (energy $\lambda = \delta_{soc}$) induces an additional splitting within the t_{2g} manifold, resulting in a $J_{eff} = 1/2$ doublet and a $J_{eff} = 3/2$ quartet, characterized by an energy of $\lambda = 3\delta_{soc}/2$. Consequently, in the hole picture, one hole is accommodated in the lower $J_{eff} = 1/2$ Kramer's doublet [17,35], as schematically shown in Fig. 1(b). Within the Mott-Hubbard framework, the $J_{eff} = 1/2$ manifold undergoes a splitting due to the Coulomb interaction U, resulting in the formation of an upper Hubbard band (UHB) and lower Hubbard band (LHB). It demonstrates that the Mott gap can exceed 2 eV, when the value of U is set to be 4.5 eV during density functional theory (DFT) calculations, as shown in the bottom panel of Fig. 1(b), which aligns favorably with the Mott gap measured via dI/dV spectroscopy and photoemission spectroscopy on bulk α-RuCl$_3$ [29,36]. The results imply that α-RuCl$_3$ is a highly correlated electron system. Several academic studies [37,38] have demonstrated that the imposition of strain or pressure upon the crystal of a Mott insulator possesses the potential to cause an insulator-to-metal Mott transition. Our prior research [29] has revealed that a minor distortion of the lattice in ML-α-RuCl$_3$ can substantially modify the electronic characteristic by causing the in-gap states within the Mott gap. A question arises of whether the
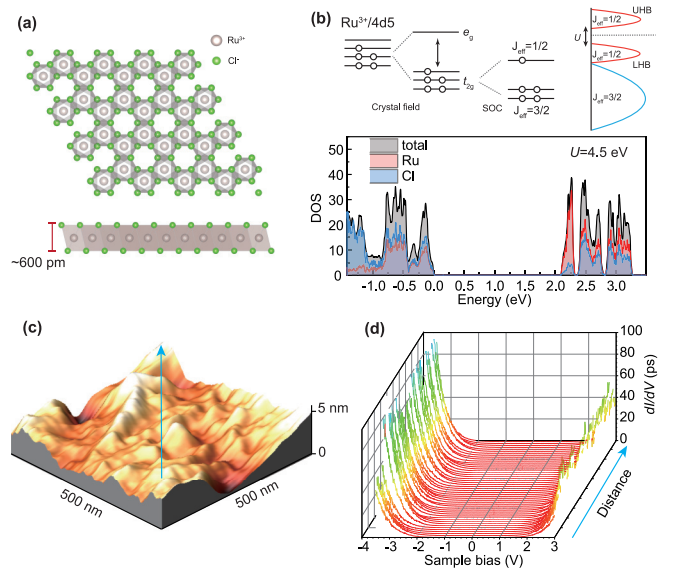
FIG. 1. (a) The in-plane and out-plane views of the crystal structure of a monolayer α-RuCl$_3$, demonstrating that an individual honeycomb layer is formed by edge-sharing RuCl$_6$ octahedra. (b) Upper panel: the level scheme of a 4d^5 electronic configuration of the ruthenium valence Ru^{3+}, where the crystal field and SOC effect together result in a $J_{eff} = 1/2$ Mott-Hubbard insulator. Lower panel: DFT calculation of the partial density of states (PDOS) of the α-RuCl$_3$ with setting $U = 4.5$ eV. The obtained Mott gap is $\sim$2 eV. (c) STM three-dimensional (3D) morphology taken on a thick α-RuCl$_3$ with clear corrugation of the film being observed. Bias voltage: $V_b = 2.5$ V; set-point current: $I_s = 500$ pA. (d) dI/dV spectra collected along the green line in (c) show that the Mott-Hubbard bands are robust. The spectra are measured with parameters $V_b = 2.5$ V and $I_s = 500$ pA, lock-in frequency of 707 Hz, and amplitude modulation of 5 mV.

applied strain or the lattice distortion possesses the capacity to trigger a Mott transition within the bulk form of α-RuCl$_3$. In this study, we exfoliated the α-RuCl$_3$ thin flakes using the Scotch tapes from a bulk single crystal synthesized from commercially available RuCl$_3$ powder by means of a vacuum sublimation. After repeatedly reducing the thickness of the film, we finally exfoliated the target α-RuCl$_3$ thin flakes using a thermal release tap in order to transfer to a fresh surface of highly oriented pyrolytic graphite (HOPG) substrate. After heating the sample to 120 °C for 20 seconds in an argon atmosphere in the glovebox, the α-RuCl$_3$ thin films were released on the graphite surface. Lattice deformation and strain of the α-RuCl$_3$ film are inevitably introduced during the transfer process. Then, the sample was directly transferred into an STM chamber and annealed at 280 °C in an ultrahigh vacuum chamber (1E-10 Torr) for at least 2 hours for degassing and improving the contacting quality prior to STM/STS measurements. We measured the thicknesses of the α-RuCl$_3$ flakes by a scanning topographic image at the step edge and measured its height profile to the graphite surface. We started by examining the condition of a thick α-RuCl$_3$ flake in the presence of the pronounced film corrugations, as demonstrated by the STM morphology in Fig. 1(c). Through the acquisition of dI/dV spectra along the designated path indicated by the

blue arrow line in Fig. 1(c), it ascertained that the large Mott gap, measured approximately to be 2 eV, remains robust over the corrugations. In contrast to the case of ML-α-RuCl$_3$ on graphite in our previous work where the in-gap states arise in the Mott gap [29], the corrugations did not give rise to any in-gap states, as shown in Fig. 1(d). This serves to validate the notion that a considerable crystal deformation is incapable of collapsing the strong Mott-Hubbard framework in bulk form α-RuCl$_3$. The viewpoint is also supported by previous calculations that the Mott-Hubbard band of α-RuCl$_3$ is hardly changed under a biaxial in-plane tensile strain of 8% [39].

B. Mott gap collapsed by the modest strain in ML-α-RuCl₃ in proximity to graphite

Subsequently, our focus was redirected towards the characteristics exhibited by the ML-α-RuCl$_3$ following its transfer onto the graphite. As depicted in the STM image in Fig. 2(a), a selected region of ML-α-RuCl$_3$ exhibits substantial film corrugations. The STM morphology was subjected to the fast Fourier transform (FFT), and the observable shifts of the Bragg peaks associated with the Ru and Cl atoms indicate that the out-of-plane corrugation has caused the in-plane distortion of the crystal lattices, as shown in the inset of Fig. 2(a). Previous studies have revealed that the lattice morphology under STM within the sample bias (V_b) range of -3.0 to 1.5 V is dominated by Ru t_{2g} and Cl p_π (p_z) orbitals, and the resulting hybridization of these orbitals gives rise to the characteristic corner-shared kagome pattern in STM images [40], which has been demonstrated in our recent experiment on bulk α-RuCl$_3$ [29]. Nevertheless, upon observation on ML-α-RuCl$_3$, it was noted that the FFT-filtered image [as shown in Fig. 2(b)] did not exhibit the anticipated kagome-like patterns. This suggests that forming the heterostructure has exerted a significant influence on the orbital configurations in ML-α-RuCl$_3$, a finding that seems to contradict the observations made on the epitaxial ML-α-RuCl$_3$ on graphite [40]. The film corrugation partitions the surface into three separate regions: region 1, characterized by a nearly strain-free lattice; region 2, where the lattice experiences compression; and region 3, where the lattice undergoes expansion, as seen in Fig. 2(b). In region 1, an intriguing observation is the existence of an area exhibiting graphenelike lattices. This observation aligns with our previous research [29], which suggests the possibility of heterointerfacial hybridization between α-RuCl$_3$ and graphite. The lattice constants for regions 1 and 3 were determined by extracting the height profile along the dashed lines, yielding the values of approximately 6 Å for region 1 and 6.4 Å for region 3, as seen in Fig. 2(c). The strain distribution across the surface has been conducted utilizing the geometric phase analysis method [41], as shown in Fig. 2(d). Subsequently, dI/dV spectra were obtained along the trajectory illustrated in Fig. 2(a), encompassing the three aforementioned regions. The results display that the large Mott gap maintains itself in region 1, whereas the Mott gap collapses within the presence of a finite local density of states (LDOS) at the Fermi level in regions 2 and 3, as shown in Fig. 2(e). Irrespective of whether the material experiences compressive or tensile strain, as depicted by the strain field maps in Fig. 2(d), the findings suggest that the
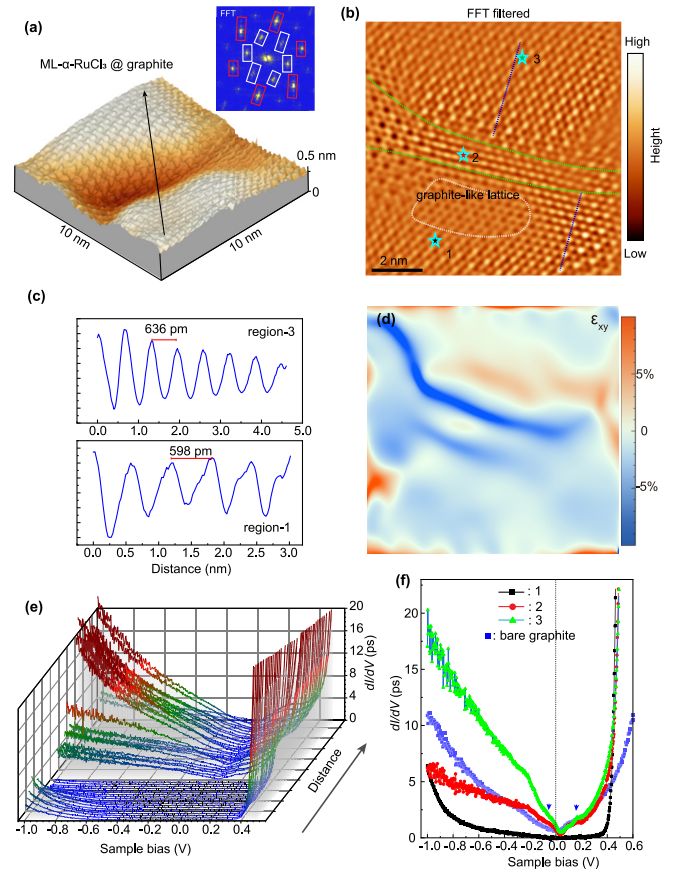
FIG. 2. (a) STM atomic-resolved morphology of ML-α-RuCl$_3$, where corrugation in the film is clearly visible; the inset show a FFT of the image, where the Bragg peaks corresponding to the Ru (white squares) and Cl (red squares) atom sites, and the strain-induced displacements of the Bragg peaks can be observed. (b) FFT-filtered STM image shows that the surface is divided into three regions (denoted as region 1, 2, and 3) by the corrugation, which present different lattice strains. (c) Height profiles along the dashes in (b) display that the lattice in region 1 has negligible distortion with a lattice constant of $a = 6$ Å, region 2 compressed, and region 3 significantly expanded with the lattice constant of $a = 6.36$ Å. (d) Strain field map obtained from geometric phase analysis represented by the ϵ_{xy} components of the strain tensors. (e) dI/dV spectra collected from the spanned surface show the evolution of band structures at 77 K, where the Mott-Hubbard gap is preserved in region 1, and the Mott gaps are collapsed in regions 2 and 3 with lattice distortions ($V_b = 500$ mV and $I_s = 500$ pA). (f) The representative dI/dV spectra acquired at 77 K from the three different regions, respectively. The blue curve underneath these spectra is the dI/dV spectrum from bare graphite.

lattice distortions induce the emergence of FS in α-RuCl$_3$. Given the negligible impact of comparable lattice distortions on the bulk film, as depicted in Figs. 1(c) and 1(d), it is highly indicative that the lattice distortions have effectively facilitated the emergence of in-gap states in ML-α-RuCl$_3$ within the heterostructure. The observed phenomenon is consistent with the theoretical calculation that applying pressure on the α-RuCl$_3$/graphene heterostructure enables the interfacial charge transfer in α-RuCl$_3$ [27]. Through the quantitative analysis with regard to the spectra observed within the three defined regions in Fig. 2(f), it was discovered that despite
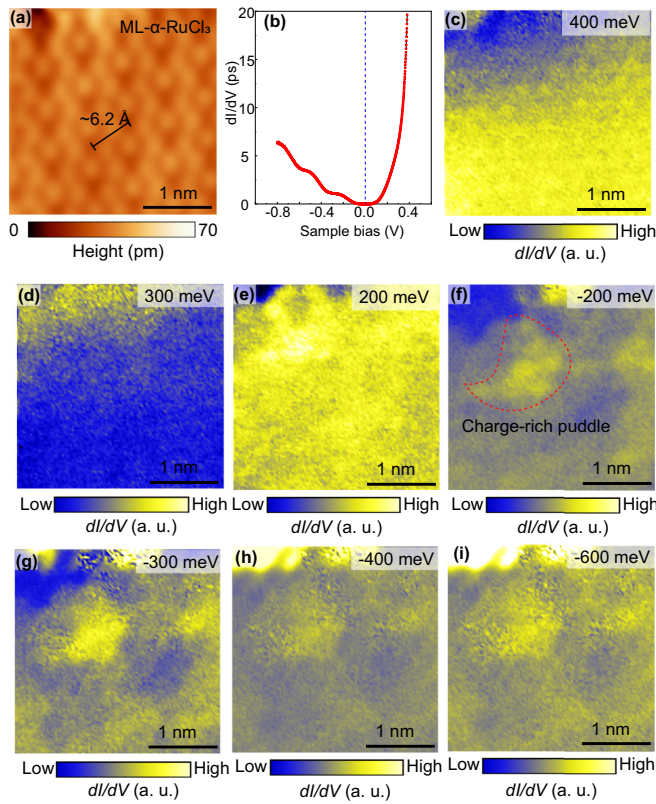
FIG. 3. (a) Atomic-resolved STM image collected on the ML-α-RuCl$_3$ with expanded lattice. (b) Averaged dI/dV spectrum acquired on the surface of (a), $V_b = 400$ mV, $I_s = 0.5$ nA. (c)–(i) Energy-dependent dI/dV maps with variation of the bias energies from 400 to -600 meV ($V_b = 400$ mV, $I_s = 1$ nA, $T = 77$ K, lock-in 707 Hz, 8 mV).

the compressed region (region 2) displaying a reduced occupied LDOS in comparison to the region subjected to tensile strain (region 3), the line shape of the spectra within both regions exhibited a remarkable similarity, rendering them nearly indiscernible. All these observed metallic dI/dV spectra exhibit a notable dip near the Fermi level, reminiscent of the pseudogap observed in the charge-doped cuprate. Then, we measured energy-resolved dI/dV maps on a ML-α-RuCl$_3$ with its lattice under modest tension ($\sim 3.5\%$), as depicted in Fig. 3(a). Figure 3(b) displays the average spectral curve, which has a nearly closed energy gap. Although the tensile strain has indeed resulted in an enhancement of the distinct states within the Mott gap, our observations in dI/dV maps [Figs. 3(c)–3(i)] have not revealed any discernible contrasts in orbital texture. This outcome aligns with our previous findings on strain-free ML-α-RuCl$_3$ [29]. It is implied that although the electrons present in α-RuCl$_3$ possess equal magnitudes to the doped holes in graphite, i.e., approximately 10^{13} cm^{-2}, these electrons have not occupied any orbitals within the energy range being examined by STS under the condition of modest lattice distortion. Consequently, it implies that the electrons in the in-gap states are itinerant or have been strongly dispersed during the tunneling process. Charge puddles can be seen in dI/dV maps that are acquired under negative energies, as shown in Figs. 3(f)–3(i). These charge puddles are thought to arise from the inhomogeneous distribution of the

electrons, which aligns with the recent theoretical prediction that the spatial distribution of the doping electrons exhibits inhomogeneity in α-RuCl$_3$ [28]. Similar charge puddles are also frequently observed in charge-doped cuprates before the emergence of the charge-ordered phase [42–45].

C. Energy-dependent orbital textures in the extremely strained ML-α-RuCl$_3$

To further elucidate the intricate interplay among lattice deformation, charge transfer, and the insulator-to-metal transition within the ML-α-RuCl$_3$ in proximity to graphite, we examined another extraordinary scenario wherein substantial biaxial strain (the lattice is shrunk over 18%) is unintentionally imposed upon a piece of ML-α-RuCl$_3$ flake, as illustrated in Fig. 4(a). Atomic-resolved STM images acquired at various sample biases, as depicted in Fig. 4(b), show a lattice morphology that exhibits similar features when the lattice is subjected to modest tensile strain, as illustrated in Fig. 2(b). The kagome-like pattern as well as the trimer pattern expected in pristine α-RuCl$_3$ were also not detected at the low-energy scale, which is a supplementary evidence notifying that the orbital configurations of ML-α-RuCl$_3$ are indeed modified upon lattice deformation and are in proximity to graphite. Moreover, the examined flake also failed to exhibit a graphite-like lattice under a bias as small as 50 mV [Fig. 4(b)], which contradicts the observations depicted in strain-free scenarios [29]. Therefore, it indicates that the electron tunneling procedure through the heterostructure has been more seriously modified.

The FFT image of the STM morphology displays the Bragg peaks corresponding to the Ru and Cl atoms, which maintains the hexagonal lattice symmetry under the strain, as depicted in Fig. 4(c). By decreasing the distance between the STM tip and the surface, hexagonal Ru atoms of the α-RuCl$_3$ lattice become clear, as shown in Fig. 4(d). Following the STM profile, Fig. 4(e) showcases that the lattice constant is 4.8 Å in this strained flake, which elucidates that the lattice is subjected to a substantial compression, exceeding -18%. The application of such a large in-plane compressive strain amplifies the out-of-plane buckling. The thickness of the present flake (500 pm), as displayed in Fig. 4(f), is greater than that of the strain-free flake (350 pm) obtained in our previous investigation [29]. It can be imagined that the significant compression in the lattice results from the thermal treatment employed during the fabrication of the heterostructure. As seen in the averaged dI/dV spectrum of the compressed lattice, as shown in Fig. 4(g), the Mott gap is thoroughly collapsed. It results in an emergence of a similar pseudogaplike feature (within the range of ± 20 meV) near the Fermi level, akin to the ones observed in Fig. 2(f). These empirical observations suggest that the application of strains may exert a systematic influence on the Mott transition. Spatially resolved dI/dV spectra along the blue arrow line in Fig. 4(d) exhibit repetitive modulation of the line shapes that aligns with the lattice's symmetry, as depicted in Fig. 4(h). This observation implies the existence of distinct orbital textures that align with the lattice geometry, potentially unveiling insights into the underlying mechanism of the strain-facilitated Mott transition. Therefore, we conducted an analysis of energy-resolved dI/dV mappings within the
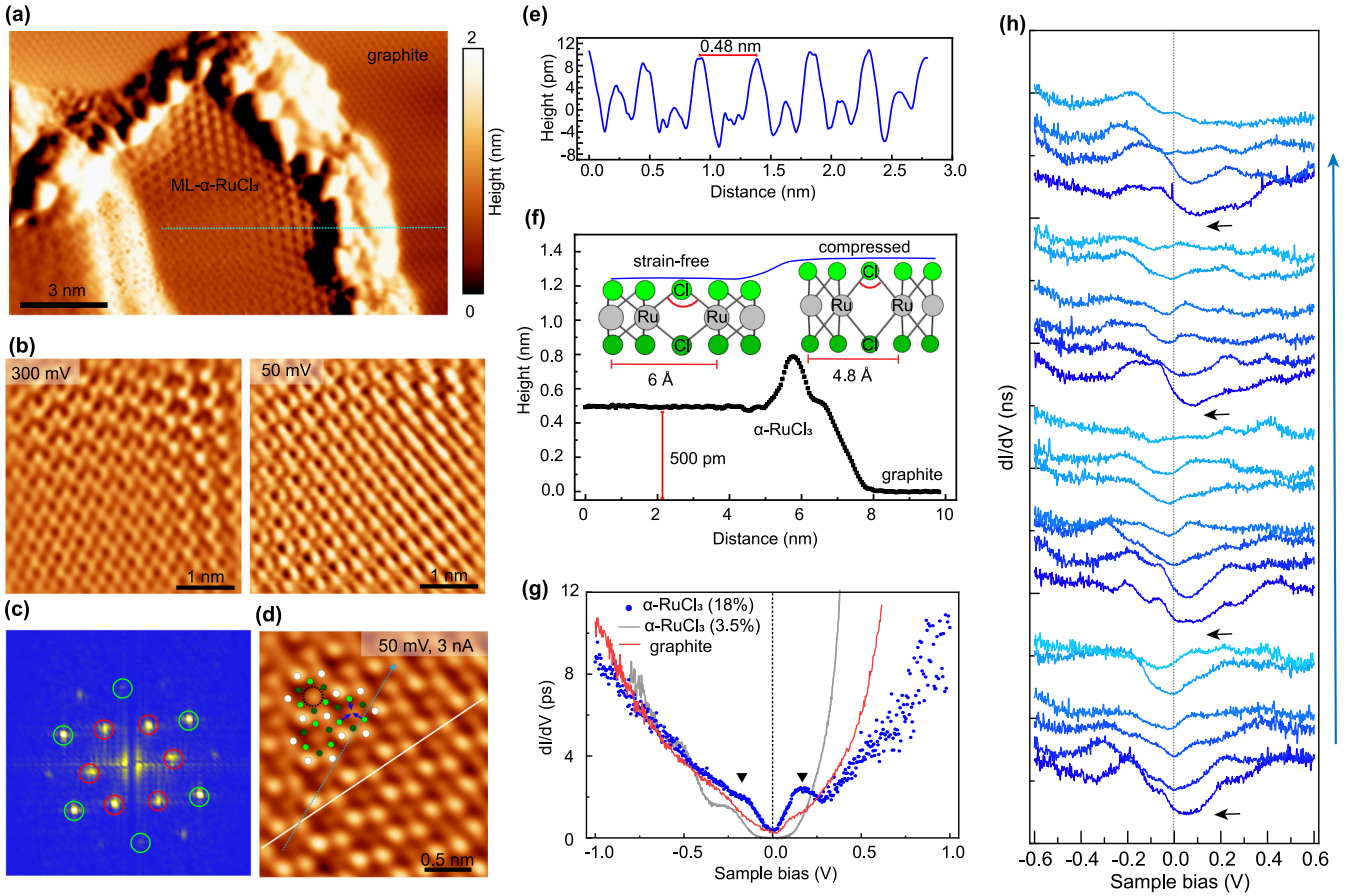
FIG. 4. (a) STM morphology of a ML-α-RuCl$_3$ flake on graphite ($V_b = 500$ mV, $I_s = 200$ pA). (b) Atomic-resolved STM images taken at different sample bias ($V_b = 300$ and 50 mV, $I_s = 1$ nA) on α-RuCl$_3$. (c) FFT image obtained from (b), where the Bragg peaks associated with the Ru and Cl atom sites maintain the hexagonal symmetry the same as the strain-free α-RuCl$_3$ film. (d) High-resolution STM morphology taken with a very small tip-surface distance setting by $V_b = 50$ mV and $I_s = 3$ nA. (e) Line profile along the white dashed line in (d) demonstrates that the lattice is significantly compressed with a lattice constant $a = 4.8$ Å, shrunk by 18%. (f) Height profile along the green line in (a) presenting the thickness of the film. (g) Comparison of averaged dI/dV spectra collected on the ML-α-RuCl$_3$ with large lattice compression ($\sim$18%), modest tension ($\sim$3.5%), and bare graphite at 77 K, respectively ($V_b = 500$ mV and $I_s = 200$ pA). (h) dI/dV spectra along the green dashed line in (d) spanning over several honeycomb lattices which reveal the atomic-resolved evolution of the LDOS on the surface ($V_b = 100$ mV, $I_s = 1$ nA, $T = 77$ K, lock-in 707 Hz, 8 mV).

defined region depicted in Fig. 4(d), encompassing an energy range spanning from 300 to −300 mV, as visually represented in Fig. 5(a). In contrast to the depicted scenario in Fig. 3, wherein the orbital texture appears indistinct, the observed region showcases remarkably discernible energy-dependent and atomically resolved orbital textures. This observation indicates that these low-energy surface electron states reside in specified orbitals within the system. The obtained dI/dV maps within the energy range reveal a remarkably diminished LDOS on Ru sites, in contrast to the pronounced concentration of high intensity in the proximity of Cl atoms. The manifestation of a weak orbital texture arising from the hybridization of Ru and Cl orbitals (t_{2g}-p_z hybridization) is confined to an energy magnitude of 40 meV. The fact that the LDOS at Cl sites exhibited a networklike pattern at the energy levels exceeding 200 meV is concurrent with a depletion of Ru sites, indicating that the pattern is predominantly composed of the Cl3p orbitals. Two distinct patterns of orbital textures are discernible when examining the occupied states. In the vicinity of the Fermi level, precisely at 0 and −20 meV

of the dI/dV maps, the LDOSs exhibit pronounced intensity patterns situated in the central region of the hexagonal lattice. In the absence of solid atomic entities occupying the central positions within the α-RuCl$_3$ lattice, we hypothesize that the central LDOSs are predominantly generated from the π bonds present on the graphite surface. Below −20 meV, the configuration of a three-pointed star within the hexagonal lattice can be observed. It can be unequivocally attributed to the 3p_z lobes of the topmost Cl atoms since they are primarily detected by the STM tip, and contribute the three-pointed star patterns to the orbital textures, as illustrated in Fig. 5(b).

The aforementioned observations demonstrate that the Cl3p orbitals are the primary source of the textures at low energies, which is paradoxical given that the low-energy electronic configuration of the α-RuCl$_3$ could be dominated by the degenerate e_g and t_{2g} bands from the Ru4d orbitals, whereas the Cl3p orbital electrons predominantly occupy the valence band below −2 eV [33,36,40]. In fact, the current observations are in agreement with the theoretical computations, which indicate that the electrons transferred from the heterointerface
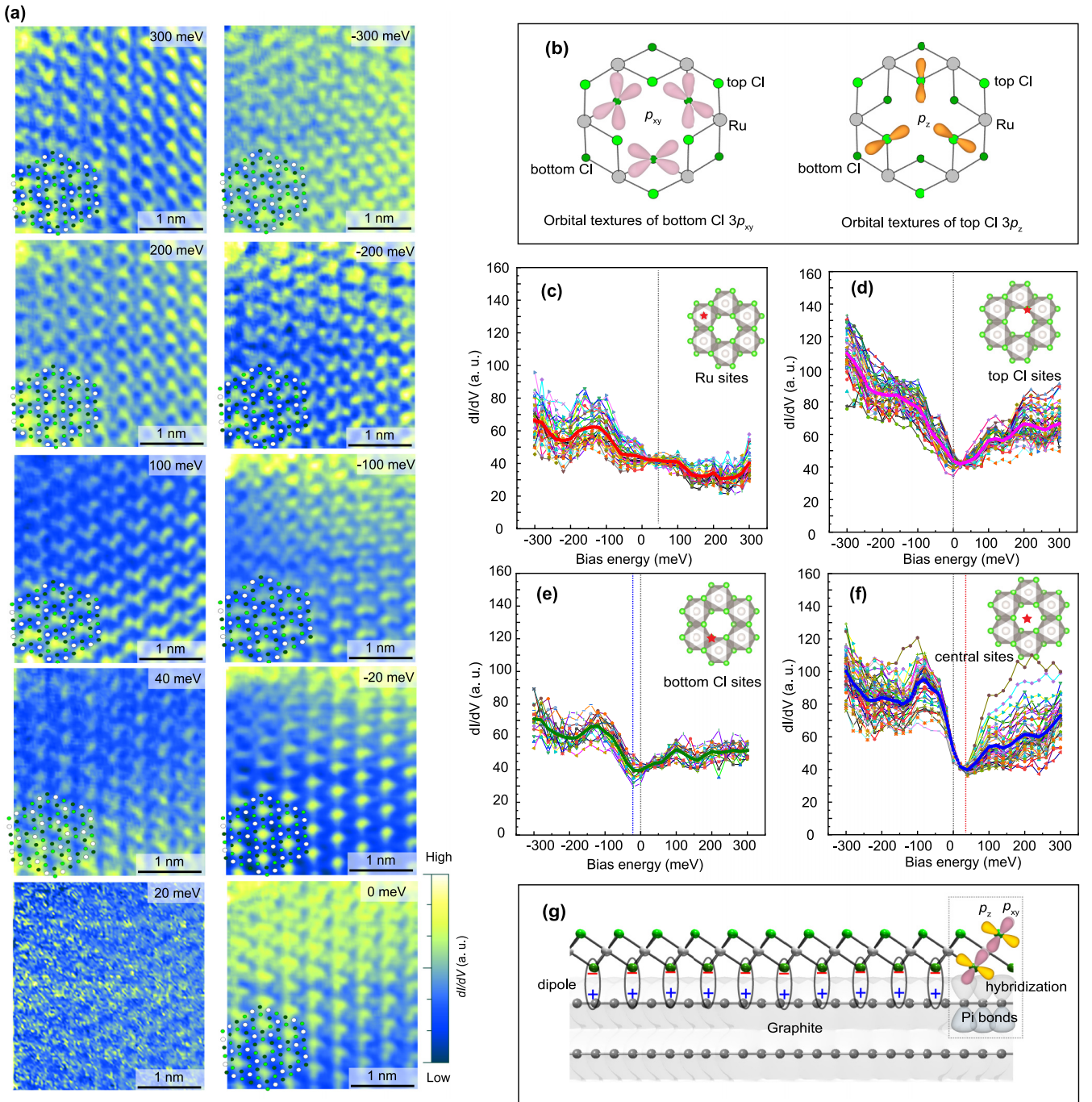
FIG. 5. (a) Energy-dependent *dI/dV* maps taken at the same region as shown in Fig. 4(d) depict the orbital textures that evolve as the changing of the energy levels. The lattice structural models are schematically put on the surfaces ($V_b = 50$ mV, $I_s = 0.6$ nA, $T = 77$ K, lock-in 707 Hz, 8 mV). (b) Schematic Cl3p orbital configurations of p_{xy} and p_z (possible orbital textures under *dI/dV* mapping) in the ML-α-RuCl$_3$. (c)–(f) The representative averaged *dI/dV* spectra collected at different sites: (c) Ru sites, (d) top-Cl sites, (e) bottom-Cl sites, and (f) center of honeycombs (as pointed out by the red stars on the lattice models), of the lattice from *dI/dV* maps in (a). (g) Schematic of interface dipoles formed between the bottom-located Cl and graphite surface, which is induced by the hybridization (charge transfer) between the Cl3p orbitals and the π orbitals of the graphite surface.

have a greater affinity for bonding to the Cl sites [28]. It suggests that the observed electron states in the orbital texture are the result of charge transfer in the heterostructure. In addition, the strain in ML-α-RuCl$_3$ has altered the electron distribution from the heterointerface to the Cl orbitals as a result of the lattice distortion.

The spatially averaged LDOS was then collected at distinct locations, specifically the Ru sites, the top and bottom Cl sites, and the sites in the center of the hexagons, as depicted in Figs. 5(c)–5(f). The LDOS curves observed at the Ru sites exhibit a nearly flat profile with a relatively reduced intensity [Fig. 5(c)]. This feature implies that the Coulomb reputation

still wishes to preserve the Mott gap in the t_{2g} band, and also explains the depletion morphology observed on the Ru sites in *dI/dV* maps in Fig. 5(a). The spectral data collected from the top and bottom Cl sites as well as the center of the hexagons all exhibit a pseudogaplike feature in the spectral curves with a minimum value near the Fermi level [as depicted in Figs. 5(d)–5(f)]. It is noteworthy that the curves originating from the bottom Cl sites present a comparatively lower intensity due to the increased tunneling distance and a negative shift of its minimum point. The spectra measured at the centers of the hexagons exhibit an asymmetric line shape, with the occupied states being significantly higher than the empty ones. In addition, as depicted in Fig. 5(f), a positive shift of the spectral minimum is observed. As was previously mentioned, the central points have the potential to provide information regarding graphite. Comparing the *dI/dV* spectra to those of bare graphite, the positive shift of the minimum can be interpreted as evidence of hole doping, which is consistent with previous findings that the graphite in the heterostructure is hole doped [23–25,46]. The negative shift of the spectral minimum at the bottom Cl sites is consistent with the band calculations [28] that the low-energy bands of the α-RuCl$_3$ shift downward in the heterostructure. As depicted schematically in Fig. 5(g), an opposite shift of the spatial spectra suggests the presence of an interfacial dipole layer between α-RuCl$_3$ and graphene [46]. The hybridization between Cl3p and π orbitals of graphite adequately accounts for the formation of the interface dipole.

This extreme case with significant lattice compression allows us to visualize the orbital structures in ML-α-RuCl$_3$ in close proximity to graphite and provides information regarding the interfacial dipoles. However, it remains unclear how the lattice distortion could cause the Mott-Hubbard band to collapse. It is essential to note that even though a large amount of electrons is transferred from graphite to strain-free ML-α-RuCl$_3$ in the heterostructure, the substantial Mott gap ($\sim$2 eV) [29] may effectively impede the movements of electrons from the heterointerface into the Mott-Hubbard band. Therefore, forming the dipole layer is reasonable, as depicted in Figs. 5(e) and 5(f). Such a proposal can accurately interpret the findings in our previous studies that the in-gap states were observable as the probing tip approaching the surface [29], and that the orbital textures on the top surface were indistinct (Fig. 3). However, by referring to the Jahn-Teller theorem and the discussion in a recent study concerning epitaxially grown α-RuCl$_3$ on graphite [40], any lattice distortion to prolong (shorten) the Ru-Ru bonds within widening (reducing) the Ru-Cl-Ru angles would cause the trigonal distortion of the Ru-Cl octahedra, as schematically depicted in Fig. 4(f) (inset).

Such distortion will cause the splitting of the t_{2g} manifold into a_{1g} singlet and e_g' doublet, while preserving the hybridization with the p_z orbitals of both the top and bottom Cl atoms. Despite the fact that α-RuCl$_3$ bulk and ML remain in the Mott-insulating state under t_{2g} splitting [39,47], the distribution of doped electrons α-RuCl$_3$ may be ultimately altered. Therefore, it is proposed with sufficient adequacy that the electrons residing at the bottom Cl layer may exhibit a higher propensity to transfer into the top Cl orbitals via the band splitting and the hybridization of p_z^{bottom}-a_{1g}-p_z^{top} and p_z^{bottom}-e_g'-p_z^{top}. The redistribution of electrons concurrently decreases the parameter U/t (t is the hopping integral) or breaks the half-filled t_{2g} band in the Mott-Hubbard framework, which collapses the Mott gap as shown in the *dI/dV* spectra in the strained ML-α-RuCl$_3$.

III. CONCLUSION

In conclusion, we reported the observation of lattice-distortion-facilitated Mott-gap collapse in ML-α-RuCl$_3$ in the heterostructure involving graphite. We clarified that the identical film deformation failed to change the Mott gap in bulk α-RuCl$_3$. Important information was provided by the energy-resolved orbital textures by conducting STM/STS measurements on an ML-α-RuCl$_3$ flake experiencing an extremely large compressed lattice strain. It was proven that a majority of charges for collapsing the Mott gap reside in the Cl3p orbitals. In order to comprehend the physical mechanism, a model was proposed that the strain causes the splitting of the t_{2g} band into a_{1g} and e_g' orbitals, and the orbital hybridization of a_{1g} and e_g' with the Clp_z greatly modifies the distribution of electrons those are transferred from graphite. Part of the electrons previously accumulated at the herterointerface (bottom Cl layer) is transferred to the upper Cl layers, via the p_z^{bottom}-a_{1g}-p_z^{top} and p_z^{bottom}-e_g'-p_z^{top} pathways under lattice deformation, resulting in the Mott transition in the context of the doped Mott-Hubbard bands. The results will provide avenues for investigating the topological superconductivity in the vicinity of a Mott transition within a Kitaev QSL candidate.

ACKNOWLEDGMENTS

[1] M. Imada, A. Fujimori, and Y. Tokura, Rev. Mod. Phys. **70**, 1039 (1998).

[2] G. Sordi, K. Haule, and A.-M. S. Tremblay, Phys. Rev. B **84**, 075161 (2011).

[3] M. Chatzieleftheriou, A. Kowalski, M. Berović, A. Amaricci, M. Capone, L. De Leo, G. Sangiovanni, and L. de' Medici, Phys. Rev. Lett. **130**, 066401 (2023).

[4] C.-H. Yee and L. Balents, Phys. Rev. X **5**, 021007 (2015).

[5] T. Hanaguri, C. Lupien, Y. Kohsaka, D.-H. Lee, M. Azuma, M. Takano, H. Takagi, and J. C. Davis, Nature (London) **430**, 1001 (2004).

[6] E. H. da Silva Neto, P. Aynajian, A. Frano, R. Comin, E. Schierle, E. Weschke, A. Gyenis, J. Wen, J. Schneeloch, Z. Xu,

S. Ono, G. Gu, M. Le Tacon, and A. Yazdani, Science **343**, 393 (2014).

[7] Y. Sakurai, M. Itou, B. Barbiellini, P. E. Mijnarends, R. S. Markiewicz, S. Kaprzyk, J.-M. Gillet, S. Wakimoto, M. Fujita, S. Basak, Y. J. Wang, W. Al-Sawai, H. Lin, A. Bansil, and K. Yamada, Science **332**, 698 (2011).

[8] P. A. Lee, N. Nagaosa, and X.-G. Wen, Rev. Mod. Phys. **78**, 17 (2006).

[9] D. Pesin and L. Balents, Nat. Phys. **6**, 376 (2010).

[10] C. Broholm, R. J. Cava, S. A. Kivelson, D. G. Nocera, M. R. Norman, and T. Senthil, Science **367**, eaay0668 (2020).

[11] L. Savary and L. Balents, Rep. Prog. Phys. **80**, 016502 (2017).

[12] Y. Zhou, K. Kanoda, and T.-K. Ng, Rev. Mod. Phys. **89**, 025003 (2017).

[13] A. Pustogow, M. Bories, A. Löhle, R. Rösslhuber, E. Zhukova, B. Gorshunov, S. Tomić, J. A. Schlueter, R. Hübner, T. Hiramatsu, Y. Yoshida, G. Saito, R. Kato, T.-H. Lee, V. Dobrosavljević, S. Fratini, and M. Dressel, Nat. Mater. **17**, 773 (2018).

[14] T. Furukawa, K. Kobashi, Y. Kurosaki, K. Miyagawa, and K. Kanoda, Nat. Commun. **9**, 307 (2018).

[15] A. Kitaev, Ann. Phys. **321**, 2 (2006).

[16] M. Gohlke, G. Wachtel, Y. Yamaji, F. Pollmann, and Y. B. Kim, Phys. Rev. B **97**, 075126 (2018).

[17] H. Takagi, T. Takayama, G. Jackeli, G. Khaliullin, and S. E. Nagler, Nat. Rev. Phys. **1**, 264 (2019).

[18] S.-M. Zhang and Z.-X. Liu, Phys. Rev. B **104**, 115108 (2021).

[19] Y.-Z. You, I. Kimchi, and A. Vishwanath, Phys. Rev. B **86**, 085145 (2012).

[20] G. B. Halász, J. T. Chalker, and R. Moessner, Phys. Rev. B **90**, 035145 (2014).

[21] M.-k. Jo, H. Heo, J.-H. Lee, S. Choi, A. Kim, H. B. Jeong, H. Y. Jeong, J. M. Yuk, D. Eom, J. Jahng, E. S. Lee, I.-Y. Jung, S. R. Cho, J. Kim, S. Cho, K. Kang, and S. Song, ACS Nano **15**, 18113 (2021).

[22] X. Zhou, H. Li, J. A. Waugh, S. Parham, H.-S. Kim, J. A. Sears, A. Gomes, H.-Y. Kee, Y.-J. Kim, and D. S. Dessau, Phys. Rev. B **94**, 161106(R) (2016).

[23] B. Zhou, J. Balgley, P. Lampen-Kelley, J.-Q. Yan, D. G. Mandrus, and E. A. Henriksen, Phys. Rev. B **100**, 165426 (2019).

[24] D. J. Rizzo, B. S. Jessen, Z. Sun, F. L. Ruta, J. Zhang, J.-Q. Yan, L. Xian, A. S. McLeod, M. E. Berkowitz, K. Watanabe, T. Taniguchi, S. E. Nagler, D. G. Mandrus, A. Rubio, M. M. Fogler, A. J. Millis, J. C. Hone, C. R. Dean, and D. N. Basov, Nano Lett. **20**, 8438 (2020).

[25] S. Biswas, Y. Li, S. M. Winter, J. Knolle, and R. Valentí, Phys. Rev. Lett. **123**, 237201 (2019).

[26] S. Mashhadi, Y. Kim, J. Kim, D. Weber, T. Taniguchi, K. Watanabe, N. Park, B. Lotsch, J. H. Smet, M. Burghard, and K. Kern, Nano Lett. **19**, 4659 (2019).

[27] E. Gerber, Y. Yao, T. A. Arias, and E.-A. Kim, Phys. Rev. Lett. **124**, 106804 (2020).

[28] P. H. Souza, D. P. de Andrade Deus, W. H. Brito, and R. H. Miwa, Phys. Rev. B **106**, 155118 (2022).

[29] X. Zheng, K. Jia, J. Ren, C. Yang, X. Wu, Y. Shi, K. Tanigaki, and R.-R. Du, Phys. Rev. B **107**, 195107 (2023).

[30] F. Iyikanat, M. Yagmurcukardes, R. T. Senger, and H. Sahin, J. Mater. Chem. C **6**, 2019 (2018).

[31] D. A. S. Kaib, S. Biswas, K. Riedl, S. M. Winter, and R. Valentí, Phys. Rev. B **103**, L140402 (2021).

[32] K. W. Plumb, J. P. Clancy, L. J. Sandilands, V. V. Shankar, Y. F. Hu, K. S. Burch, H.-Y. Kee, and Y.-J. Kim, Phys. Rev. B **90**, 041112(R) (2014).

[33] W. Lu, H. Lee, J. Cha, J. Zhang, and I. Chung, Angew. Chem. **135**, e202219344 (2023).

[34] A. Koitzsch, C. Habenicht, E. Müller, M. Knupfer, B. Büchner, H. C. Kandpal, J. van den Brink, D. Nowak, A. Isaeva, and T. Doert, Phys. Rev. Lett. **117**, 126403 (2016).

[35] G. Jackeli and G. Khaliullin, Phys. Rev. Lett. **102**, 017205 (2009).

[36] S. Sinn, C. H. Kim, B. H. Kim, K. D. Lee, C. J. Won, J. S. Oh, M. Han, Y. J. Chang, N. Hur, H. Sato, B.-G. Park, C. Kim, H.-D. Kim, and T. W. Noh, Sci. Rep. **6**, 39544 (2016).

[37] K. Bu, W. Zhang, Y. Fei, Z. Wu, Y. Zheng, J. Gao, X. Luo, Y.-P. Sun, and Y. Yin, Commun. Phys. **2**, 146 (2019).

[38] K. Dymkowski and C. Ederer, Phys. Rev. B **89**, 161109(R) (2014).

[39] E. Vatansever, S. Sarikurt, F. Ersan, Y. Kadioglu, O. Üzengi Aktürk, Y. Yüksel, C. Ataca, E. Aktürk, and Ü. Akıncı, J. Appl. Phys. **125**, 083903 (2019).

[40] Z. Wang, L. Liu, M. Zhao, H. Zheng, K. Yang, C. Wang, F. Yang, H. Wu, and C. Gao, Quantum Front. **1**, 16 (2022).

[41] M. J. Hÿtch, E. Snoeck, and R. Kilaas, Ultramicroscopy **74**, 131 (1998).

[42] P. Cai, W. Ruan, Y. Peng, C. Ye, X. Li, Z. Hao, X. Zhou, D.-H. Lee, and Y. Wang, Nat. Phys. **12**, 1047 (2016).

[43] I. Battisti, K. M. Bastiaans, V. Fedoseev, A. de la Torre, N. Iliopoulos, A. Tamai, E. C. Hunter, R. S. Perry, J. Zaanen, F. Baumberger, and M. P. Allan, Nat. Phys. **13**, 21 (2017).

[44] E. H. da Silva Neto, B. Yu, M. Minola, R. Sutarto, E. Schierle, F. Boschini, M. Zonno, M. Bluschke, J. Higgins, Y. Li, G. Yu, E. Weschke, F. He, M. Le Tacon, R. L. Greene, M. Greven, G. A. Sawatzky, B. Keimer, and A. Damascelli, Sci. Adv. **2**, e1600782 (2016).

[45] A. Frano, S. Blanco-Canosa, B. Keimer, and R. J. Birgeneau, J. Phys.: Condens. Matter **32**, 374005 (2020).

[46] A. Rossi, C. Johnson, J. Balgley, J. C. Thomas, L. Francaviglia, R. Dettori, A. K. Schmid, K. Watanabe, T. Taniguchi, M. Cothrine, D. G. Mandrus, C. Jozwiak, A. Bostwick, E. A. Henriksen, A. Weber-Bargioni, and E. Rotenberg, Nano Lett. **23**, 8000 (2023).

[47] L. Liu, K. Yang, G. Wang, D. Lu, Y. Ma, and H. Wu, Phys. Rev. B **107**, 165134 (2023).